Mu, N., Schulz, H.-M., Fu, Y., Schovsbo, N. H., Wirth, R., Rhede, D., van Berk, W. (2015): Berthierine formation in reservoir rocks from the Siri oilfield (Danish North Sea) as result of fluid-rock interactions: Part I. Characterization. - *Marine and Petroleum Geology*, *65*, p. 302-316.

DOI: http://doi.org/10.1016/j.marpetgeo.2015.04.010

Berthierine formation in reservoir rocks from the Siri oil field (Danish North Sea) as result of fluid-rock interactions: Part I. Characterization

Nana Mu[1], Hans-Martin Schulz[1], Yunjiao Fu[1], Niels Hemmingsen Schovsbo[2], Richard Wirth[3], Dieter Rhede[4], and Wolfgang van Berk[5, *]

[1]Helmholtz Centre Potsdam − GFZ German Research Centre for Geosciences, Section 4.3, Organic Geochemistry, Telegrafenberg, D-14473 Potsdam, Germany

[2]Geological Survey of Denmark and Greenland, Øster Voldgade 10, DK-1350 Copenhagen K, Denmark

[3]Helmholtz Centre Potsdam - GFZ German Research Centre for Geosciences, Section 3.3, Chemistry and Physics of Earth Materials, Telegrafenberg, D-14473 Potsdam, Germany

[4]Helmholtz Centre Potsdam - GFZ German Research Centre for Geosciences, Section 4.2, Inorganic and Isotope Geochemistry, Telegrafenberg, D-14473 Potsdam, Germany

[5]Department of Hydrogeology, Clausthal University of Technology, Leibnizstraße 10, D-38678 Clausthal-Zellerfeld, Germany

*Corresponding author: Tel.: +49-5323-72-2234; Fax: +49-5323-72-2903; Email address: wolfgang.van.berk@tu-clausthal.de

ABSTRACT

Berthierine as the only authigenic Fe-rich clay mineral occurs in an oil-bearing, glauconite-rich sandstone (Paleocene Heimdal Member of the Lista Formation, Danish North Sea). Based on the results of thin section, transmission and scanning electron microscopy, five different morphological types of berthierine were identified: (1) mainly as grain-coatings partly together with authigenic quartz covering detrital grains, (2) as pore-filling clay in open pores, (3) small crystals in transformed glauconite grains; (4) small crystals associated with siderite in layers of mica/micaceous glauconite; and (5) as elongated crystals in siderite concretions. Although different in occurrence, all berthierine types investigated by microprobe analysis are of similar chemical composition, suggesting similar precipitation conditions. Investigations by transmission electron microscopy reveal that fine berthierine crystals display straight parallel layers with a typical lattice fringe spacing of 0.7 nm, and that their occurrence is intimately connected to oil phases in pore space. Partly, berthierine textures resemble mineralized oil-water emulsions. Berthierine is more abundant in the oil leg than in the water leg, but occurs especially abundant at the oil-water contact. The coexistence of berthierine together with quartz overgrowth, but also its appearance in glauconite indicates that berthierine formed *in situ* and that it is a product of glauconite dissolution. Berthierine formation is coupled to the reduction of aqueous Fe^{3+} into Fe^{2+} derived from glauconite dissolution, and is related to fluid-rock interactions triggered by oil degradation which occurred in the oil-filled zone and at the oil-water contact. The biomarker parameters pristane/*n*-C_{17} and phytane/*n*-C_{18} indicate an increased extent of oil degradation at the oil-water contact. On the one hand, soluble oil degradation products (methane, carbon dioxide, and hydrogen) changed the hydrogeochemical conditions (such as pH, pe, alkalinity, etc.), and controlled dissolution of glauconite (and feldspar). On the other hand, the changed hydrogeochemical conditions led to berthierine and quartz precipitation in water-wet reservoir

intervals.

1. Introduction

Berthierine is an aluminous Fe^{2+}-rich 1:1-type layer silicate with a basal spacing of 0.7 nm, belonging to the kaolinite-serpentine group (Kodama and Foscolos, 1981; Damyanov and Vassileva, 2001; Worden and Morad, 2003; Wise, 2007). Alternative or ancient names for this mineral are septechlorite, septechamosite, chamosite, 0.7 nm-chamosite, and/or 0.7 nm-chlorite (Hornibrook and Longstaffe, 1996).

Berthierine is composed of Al_2O_3 (28−12 wt.-%), SiO_2 (19−27 wt.-%), FeO (32−37 wt.-%), and minor portions of Fe_2O_3 and MgO, and chemically and crystallographically resembles iron-rich chlorite (chamosite; Brindley, 1982; Hornibrook and Longstaffe, 1996). Conventional XRD methods are limited to unequivocally detect berthierine in mixtures with chlorite or whether exclusively chlorite prevails. However, heating samples causes the disappearance of the 1.4 nm basal reflection on XRD patterns that is characteristic of chlorite (Brindley, 1982; Rivas-Sanchez et al., 2006). Heating, furthermore, leads to an increase of the 0.73 nm peak of chlorite, whereas this peak weakens in berthierine because of sheet breakdown (Deer et al., 1992). In addition, transmission electron microscopy (TEM) can also be applied to distinguish berthierine from chlorite by the absence of 1.4 nm and the presence of 0.7 nm, dhkl [001] basal spacing in lattice fringes (Coombs et al., 2000; Rivard et al., 2013; Rivas-Sanchez et al., 2006).

Berthierine is chemically and structurally also similar to the 1:1-layer silicate odinite. Similarities are the basal spacing of 0.7 nm, and many identical XRD lines (Bailey, 1988; Huggett and Gale, 2002; Odin, 1990). In contrast to odinite, berthierine may have higher alumina contents, but less Mg and Si contents (Hornibrook and Longstaffe, 1996). In addition, berthierine is rich in ferrous iron (Fe^{2+}) whereas odinite contains dominantly ferric iron (Fe^{3+}). Therefore,

berthierine is less likely to be misidentified as odinite in ancient sedimentary rocks.

Berthierine frequently occurs in marine-oolitic ironstone formations. Prominent examples are berthierine ooids in the marine Lower Miocene strata of the Tenggol Arch area, offshore Peninsular Malaysia (Madon, 1992), or ooids and fine berthierine crystals together with siderite in the marine Jurassic ironstone-mudstone succession, UK (Taylor and Curtis, 1995), to name but two. However, berthierine may also occur in non-marine sedimentary strata such as arctic desert soil (Kodama and Foscolos, 1981), laterite (Toth and Fritz, 1997), coal measures (Iijima and Matsumoto, 1982), and sediments deposited in brackish water (Rohrlich et al., 1969; Taylor, 1990). Apart from sedimentary environments, inferred hydrothermal berthierine has been observed in altered mafic rocks (Ruotsala et al., 1964), sedimentary exhalative siderite iron formations (Damyanov and Vassileva, 2001), volcanogenic massive sulfide deposits (Slack et al., 1992), and in granitic pegmatites (Wise, 2007). A detailed compilation of berthierine occurrences was presented by Toth and Fritz (1997).

In contrast, the occurrence of berthierine in sandstone reservoirs was rarely reported, e.g., in oil sands of the Lower Cretaceous Clearwater Formation in Alberta, Canada (Hornibrook and Longstaffe, 1996), in the Greensand Formation of the Late Cretaceous Sherbrook Group, Otway Basin, Australia (Boyd et al., 2004), and in the Paleocene Hermod sandstone of the Stine segment in the Siri field (Stokkendal et al., 2009). Interestingly berthierine formation in the Upper Jurassic Georgiev Formation was probably controlled by products of organic matter diagenesis in the overlying Lower Cretaceous Bazhenov Formation (Sánchez-Navas et al., 2008) which is the main source rock for oil and gas fields in the Western Siberian Basin. In addition, berthierine has been documented in the Burgess Shale as a coating on organic remains, which are assumed to be diagenetic oxidation products of organic matter in the iron-reducing pathway (Petrovich, 2001).

The present contribution builds on existing findings and assumptions for the Paleocene

siliciclastic oil (and gas) reservoirs in the Danish North Sea (e.g., Stokkendal et al., 2009). In the glauconite-rich sandstone reservoirs of the Paleocene Heimdal and Hermod members in the Siri field, berthierine mainly occurs as grain coating in close association with siderite, glauconite, and –importantly– also with oil and gas fillings (details in section 5). This specific mineral assemblage in oil-filled reservoirs offers a window of opportunity to study intimately interconnected organic-inorganic processes that may lead to berthierine formation due to oil degradation and related petroleum-water-rock-gas interactions.

It is the conceptual approach of this first part of three companion manuscripts (Part II by Fu et al., 2015a; Part III by Fu et al., 2015b) to characterize berthierine in terms of shape (morphology, structure), crystallographic structure and chemical composition together with the mineralogical framework of the hosting oil-stained sandstone reservoir. It is the aim to elaborate a first qualitative pathway about fluid-rock interactions leading to berthierine formation based on the applied methodology including light microscopy, scanning electron microscopy (SEM), transmission electron microscopy (TEM), X-ray diffraction (XRD) and electron microprobe analysis (EMPA). The descriptive results will raise overall questions about the genetic pathways and on quantitative aspects of berthierine formation due to organic-inorganic interactions in an oil reservoir.

2. Physicochemical conditions of berthierine formation– a brief review

The different genetic pathways leading to berthierine precipitation are still a matter of debate. The generally favored concept is that berthierine forms in a reducing environment during early diagenesis by replacement or modification of a precursor (Hornibrook and Longstaffe, 1996). Odinite is regarded as the most frequent precursor, because it is chemically similar to berthierine (Odin, 1990) and could evolve to berthierine during early diagenesis by a loss of Mg and

reduction of Fe^{3+} to Fe^{2+} (Huggett and Hesselbo, 2003). Moreover, kaolinite was proposed to be another precursor for berthierine in ironstones (Bhattacharyya, 1983) and in Triassic soils (Sheldon and Retallack, 2002). Under laboratory conditions diagenetic transformation of Fe(III) oxyhydroxides to berthierine has also been achieved (Harder, 1978, 1989). However, Maynard (1986) suggested that the process of precursor replacement relies on a complete dissolution followed by re-precipitation rather than a simple addition of divalent cations to kaolinite and its structural reformation. In contrast to rather general concepts, Van Houten and Purucker (1984) proposed that berthierine formation was caused by neoformation, with the evidence of grain-coating, pore- and void-filling berthierine.

Even though berthierine may form under different conditions and in different geological settings, its manifold occurrence reveals similar physicochemical conditions during formation. The most important controlling factor for berthierine formation is a reducing environment. For example, Taylor and Macquaker (2011) stated that iron reduction predominated in marine shelf systems with consequently changed pore water composition, leading to the precipitation of iron-bearing clay minerals such as berthierine in the absence of sulfide. Another example is the formation of pore-filling Fe-berthierine in a Cretaceous laterite under reducing conditions which were established by downward percolation of organic-rich waters derived from swamps (Toth and Fritz, 1997). Moreover, it is important to note that pore-lining berthierine formed in oil sands of the Clearwater formation. The reducing environment for berthierine formation in the oil sands is argued to be due to intense microbial activity (Hornibrook and Longstaffe, 1996). In summary, thermodynamic calculations based on a study of a Cretaceous Fe-berthierine-bearing laterite (Fritz and Toth, 1997) further revealed that berthierine precipitation is favored by solutions having: (1) low Mg^{2+}/Fe^{2+} ratios; (2) extremely low sulfate contents in formation water before reduction takes place; and (3) moderately reducing conditions.

3. Geological setting and mineralogical framework

The Siri oil field is located in the Siri Canyon, which was part of a larger system of submarine canyons. The canyons developed during the Paleocene in the Norwegian-Danish Basin and today extend towards the North Sea Central Graben (Fig. 1; Huuse, 1999; Hamberg et al., 2005). The Siri Canyon sedimentary rocks consist of deep marine pelagic to hemipelagic marlstones and shales that contain a series of back stepping sandstones. The youngest sandstones are represented by the Bor and Tyr members in the Våle Formation. The youngest are the Heimdal and Hermod members embedding in the Lista and Sele Mudstone formations (Hamberg et al., 2005; Stokkendahl et al., 2009). These sediments were deposited on eroded Late Cretaceous chalk rock and are –in turn– conformably overlain by marine shales of the Sele Formation (Poulsen et al., 2007). Sourced from the Stavanger Platform, the glauconite-bearing sands were transported by gravity flows through the submarine canyon to their present-day location (Danielsen et al., 1995; Hamberg et al., 2005). The source rocks for the hydrocarbons in the Siri field are the Middle Jurassic coaly Bryne Formation, and the Upper Jurassic Farsund and Mandal Formations in the Central Graben. Petroleum migration from Jurassic source rocks in the Central Graben into Paleocene sandstones took place along the Coffee Soil Fault and vertically through the Late Cretaceous chalk. The first oil charge took place during the Late Paleogene-Early Neogene when the Heimdal sandstone was buried to approximately 1,000m depth (Hamberg at al., 2005; Ohm et al., 2006). A regional Fennonscandian uplift resulted in leakage and remigration of oil in the Siri field due to the tilted palaeo oil-water contact (OWC). Petroleum from the shallow Søgne Basin is believed to enter the Siri field quite recently. In the Siri field, the present burial depths of the Heimdal sandstone are around 2,150m and the bottom temperature is approximately 79°C. Burial history reconstructions suggest that the maximum depth and temperature did not exceed the

current burial depth and temperature. The produced oil in the Siri field has API gravities of more than 35° (Ohm et al., 2006), and the water saturation of the Heimdal Member is as high as 30−40% in the oil leg (data from Siri field).

4. Methods

Prior to preparations, all core samples were extracted for 24 hours using 99 *n*-hexane: 1 dichloromethane in a Dionex ASE 200 soxhlet at 50°C in order to remove freely accessible hydrocarbons. However, the treated core samples still contained residual oil in small, isolated pores (e.g., Figs. 2c, 2e). 24 extracted samples taken from the gas cap, the oil leg, the OWC and the underlying water leg were selected for preparation of thin sections. All these sections were stained with blue-dyed epoxy and later microscopically studied under white and UV light. Six thin sections selected each from the gas cap, the oil leg, the oil-water contact and the water leg were coated with carbon for further investigations by SEM using scanning (SE) and backscattered scanning electron (BSE) modes. 600 point counted data were obtained from nine thin sections using transmitted light microscope images. Using freshly broken chips, the micromorphology of berthierine was determined under a Philips SEM-515 with an Edax PV 9100 energy-dispersive X-ray spectroscopy (EDS) system, operated at 30 kV. To further identify berthierine, the clay fraction of sample powders was analyzed by XRD. Clay fractions were prepared by mechanical separation, followed by adding distilled water into sample powder, ultrasonic treatment, piping the upper part of the liquid into glass containers after 1-2 minutes of settling, and lastly air-drying at room temperature. XRD analyses of the clay fractions were conducted applying a PHILIPS PW 1820 device, using Cu Kα radiation (35Kv, 35 mA). Scans were run between 2 and 36°, 2ɵ with a step size of 0.013° in the air-dry state.

Berthierine and its mineral matrix filled by residual oil were further investigated by TEM. Samples for TEM were cut from pre-defined areas in the polished thin sections by focused Ar-ion beam (FIB) milling in an ultrahigh vacuum using a FEI FIB200 instrument (for more details see Wirth, 2004, 2009). These ultrathin samples were analyzed using a FEI Tecnai G2 F20 X-Twin TEM, equipped with a field-emission electron source (operated at 200 kV), a Fishione high-angle annular dark-field detector (HAADF), a Gatan Tridiem imaging filter for acquisition of energy-filtered images, and an EDAX Genesis X-ray analyzer with an ultrathin window. The characterization of samples included bright-field/dark-field imaging, high-resolution imaging, electron diffraction, and EDX analyses (in scanning-TEM mode).

For determining the qualitative chemical composition of berthierine, two selected thin sections from the oil leg and the water leg were coated with carbon for EMPA. The major element chemistry of berthierine was determined using wavelength-dispersive analysis by a JEOL field emission gun JXA-8500F electron microprobe operating at 20 kV, with a beam current of 10 nA and a beam diameter of 1−5 µm or focus beam depending on berthierine grain sizes. The peak counting times were 20−30 s and the background counting times were always set to half of the respective peak counting times. The structural formula for berthierine was calculated on the basis of 7 oxygens.

For biomarker analysis a total of twelve core extracts were selected from the gas cap, the oil leg and the OWC. All extracts were separated into maltenes (*n*-hexane-soluble fraction) and asphaltenes by asphaltene precipitation using a hexane-dichlormethane solution. The *n*-hexane-soluble fractions were furthermore separated into saturated hydrocarbons, aromatic hydrocarbons and resins using medium-pressure liquid chromatography (MPLC). The aliphatic fractions were analyzed using GC-FID (flame ionization detection) to obtain distribution patterns in the *n*-C_{15} to *n*-C_{30} range. The GC-FID instrument was equipped with a HP Ultra 1 capillary column, using He

as carrier gas. The oven temperature was programmed from 40°C (2 min isothermal) to 300°C (65 min isothermal) at 5°C/min heating rate. The identification of individual compounds was accomplished on the basis of retention times.

5. Results

5.1. Petrography of Heimdal sandstone

The Paleocene Heimdal Member is characterized by 30−100m thick beds of olive-green to greenish gray, fine to very fine-grained, well-sorted glauconitic sandstones. The glauconitic sandstones are of uniform grain size, sorting and mineralogical composition, containing 40 vol.-% of glauconite, 30 vol.-% of quartz and 15 vol.-% of feldspar (Table 1, Fig. 2). Glauconite mainly occurs as rounded grains (Fig. 2e), but also as micaceous glauconite which has mica cleavages (Fig. 2g). Mica (mainly muscovite) is a minor component. Pyrite, zircon, rutile and Fe-Ti oxides occur as accessory minerals. Authigenic minerals include quartz overgrowth, kaolinite, siderite, berthierine and calcite (Table 1, Fig. 2).

Main diagenetic phenomena in the Heimdal sandstone are quartz overgrowth, feldspar and glauconite dissolution, berthierine precipitation, and calcite cementation (all illustrated in Fig. 2). Authigenic quartz commonly occurs in form of an overgrowth rim on detrital quartz grains (Fig. 2a) and also as microcrystalline quartz on the surface of detrital grains, such as glauconite and feldspar. The interfaces between quartz overgrowth and detrital quartz always contain dark margins (Figs. 2a, 2d), which were proven to be residual oil or small petroleum inclusions by their yellow fluorescence under UV illumination. Obviously, quartz overgrowth often co-exists with berthierine (Figs. 2d, 4c and 4d). Detrital feldspar grains including K-feldspar and albite display different stages of dissolution from slight to nearly complete dissolution (Figs. 2a, 4b, 5f).

Calcite as pore-filling cement may account for up to 36 vol.-% at the OWCs (Table 1) and may completely occlude pores (Figs. 2b, 2e), which significantly reduces porosity and permeability. Calcite cement is a late stage diagenetic phase, postdating oil filling and other diagenetic processes. This cement precipitated on quartz overgrowth, after dissolution of feldspar and glauconite with bitumen rims, and after precipitation of authigenic berthierine and glauconite with bitumen rim (Figs. 2b, 2e). Siderite in the Heimdal sandstone occurs as large concretions (Fig. 2b) or as small subhedral crystals in pores (Fig. 2b), but also in mica together with berthierine and residual oil (Figs. 2c, 4d) and in micaceous glauconite (Figs. 2g, 2h).

Berthierine, the most important diagenetic phase, is present in all samples and has the highest amount (7 vol.-%) at the OWC (Table 1). Even though berthierine is quite similar to chlorite in terms of texture and chemical composition, only berthierine (no chlorite) in the Heimdal sandstone was determined by the exclusive presence of a 0.7 nm peak and the absence of a 1.4 nm peak in XRD diagrams (Fig. 3). Berthierine was further proven based on its 0.7 nm lattice reflection by TEM (Figs 6e, 7d and 7f) and its chemical composition by EMPA (Fig. 8). In thin sections, berthierine was identified by its brown (Figs. 2d, 2f) to brown-green color (Figs. 2e, 2g).

Berthierine also shows close proximity to dissolved glauconite, mica and residual oil/bitumen. Glauconite grains may be surrounded by black residual solid bitumen, showing an obviously lighter green fabric structure in-between (Fig. 2e), which is –at higher magnification– a berthierine belt (Figs. 4a, 5c). In addition, berthierine was also observed in dissolved glauconite (Figs. 2f, 5a) and close to dissolved micaceous glauconite which has micaceous layers and siderite in between (Figs. 2g, 2h).

5.2.Berthierine typing in the Heimdal sandstone

Five different types of berthierine were distinguished based on morphology and their relation to other minerals: (1) as grain coatings partly with or without quartz overgrowth covering detrital grains (Figs. 4, 5f); (2) as pore fillings (Figs. 2d, 2f and 5c); (3) as blade-like crystals in detrital glauconite grains (Figs. 5a, 5b); (4) in layers of mica or micaceous glauconite associated with siderite (Figs. 5c, 5d); and (5) in siderite concretions (Figs. 5e, 7a). Although different in occurrence, they all are of 1−2 μm size and have a similar chemical composition (Fig. 8).

Type 1 berthierine appears in the form of grain coating, and is the most frequent type. It can be subdivided into four different (I-IV) morphological subtypes. Subtype I berthierine coating exclusively covers glauconite grains except for grain-grain contacts (Fig. 4a), which indicates that berthierine coating formed after burial compaction. This berthierine subtype occurs throughout the reservoir, but is more abundant in the oil leg and at the OWC (Table 2). Subtype II berthierine occurs in or on dissolved feldspar (Figs. 4b, 5f). Subtype III berthierine coats detrital quartz together with quartz overgrowth (Figs. 4c, 4d), showing a genetic relationship with quartz overgrowth. This subtype is the most common one, and -as for subtype I- predominates in the oil leg and at the oil-water contact. Subtype IV berthierine forms as network coatings together with pyrite framboids (Fig. 4e) or occurs together with quartz overgrowth (Fig. 4f). The berthierine net coating on microquartz overgrowth in Figure 4f indicates that berthierine formation may postdate quartz growth. This berthierine type is less common and restricted to few samples from both the oil and the water leg (Table 2).

Type 2 berthierine is as pore-filling cement (Figs. 2d, 2f, 2g), which is absent at grain-grain contacts (Figs. 2d, 2f) and which is cemented by calcite (Fig.5c). The pore-filling berthierine is also abundant at the OWC (Table 2).

Type 3 berthierine is characterized by 1−2μm sized crystals forming in glauconite. This berthierine type occurs together with lath shape mica (10−20 μm long and 1−3 μm wide; Fig. 5b).

Importantly, Type 3 berthierine was also observed in strongly dissolved glauconite grains (Figs. 2f, 5a). Detailed TEM studies show that berthierine type 3 grows into the residual oil phase (Figs. 6c) and close to mineralized oil-water emulsions (Figs. 6f, 6g). Type 3 berthierine is more abundant in the oil leg, especially near the current OWC (Table 2).

Type 4 berthierine occurs between and on individual lamellae of mica/micaceous glauconite together with siderite crystals (Figs. 5c, 5d). Mica lamellae may be covered by berthierine crystal layers of 0.5μm width and berthierine also prevails as blade crystals (2−3 μm) together with authigenic fine siderite crystals (1−5 μm) in pores between mica lamellae. This type 4 berthierine was observed in the gas cap, in the oil leg and at the OWC (Table 2).

Type 5 berthierine exclusively fills pores of siderite concretions as fine blade crystals (1−2 μm) which appear perpendicular to siderite crystals (Figs. 5e, 7a and 7b). Importantly, the pores in siderite concretions contain residual immobile oil (Figs. 7a, 7b). This type 5 berthierine is closely associated with siderite concretions which only occur in several depth intervals of the oil leg (Table 2).

In summary, the five berthierine types occur in all parts of the Heimdal Member, but are concentrated in the oil leg and at the oil-water contact rather than in the gas cap or the water leg. However, the highest amounts of total berthierine were observed in samples from the OWC (Table 2).

5.3.TEM studies about berthierine formation in the presence of oil

Detailed TEM studies were carried out to further investigate the potential relationship between authigenic berthierine, specific characteristics of oil phases and associated minerals. The FIB sections were cut from characteristic interfaces observed in thin sections where residual oil was trapped in small pores or where oil-stained minerals or oil-stained mineral assemblages were

present.

The TEM investigations highlight that berthierine crystals are intimately associated with glauconite, siderite, quartz, and mica, but that there is also a direct relationship with the co-occurring oil phases. Berthierine crystals were precipitated close to glauconite in nanopores which are filled with degraded oil and/or mineralized oil-water emulsions (Fig. 6; sample from the OWC). Berthierine crystals formed on the surface of siderite crystals and bridge them, but also precipitated in oil-filled pores (Figs. 7a-d; sample from the oil leg). Berthierine crystals also formed together with siderite crystals in oil-filled pores between lamellae of mica and also as thin layers in lamellas. Furthermore, they are associated with secondary quartz precipitates in oil-filled pores (Figs. 7e-g; sample from the gas cap).

In summary, berthierine in the Heimdal Member of the Lista Formation formed as a 0.7 nm iron-rich phyllosilicate, a berthierine-1H (a Fe-serpentine after Brindley, 1982; see insert in Figs. 6e, 7d, 7f, and SAED pattern in Fig. 7g). The nanometer-sized berthierine crystals display an intimate relation to oil in pores. Such oil can occur as localized and pure single phase (e.g., in Figs. 6c, 7a, 7e) or structurally resemble mineralized oil-water emulsions (Fig. 6f).

5.4.Chemical composition of berthierine

The results of representative microprobe analyses of six berthierines crystals from the oil leg and three from the water leg are given in Table 3. Berthierine is predominantly composed of Fe with only minor variations (34.14−38.19 wt.-% FeO), which is consistent with most analyses found in the literature. However, SiO_2 (27.6−30.36 wt.-%) and Al_2O_3 contents (19.49−22.2 wt.-%) show small variations, whereas MgO contents vary from 3.08 wt.-% to 5.24 wt.-%. Other elements (given as oxides), such as MnO, CaO, Na_2O and K_2O, occur in minor concentrations. It is important to note that all nine investigated berthierine crystals are chemically similar. The

overall chemical similarity of berthierine in this study indicates that berthierine precipitation in the oil and water leg of the Heimdal reservoir took place under similar hydrogeochemical conditions. However, they compositionally differ from berthierine crystals reported in other studies (Brindley, 1982; Hornibrook and Longstaffe, 1996; Lu et al., 1994; Stokkendal et al., 2009; Toth and Fritz, 1997; Fig. 8). Berthierine crystals investigated in this study are enriched in Si^{4+} compared to berthierine in the Clearwater formation (Hornibrook and Longstaffe, 1996), and are enriched in Al^{3+} and Fe^{3+} compared to berthierine in the Hermod sandstone (Stokkendal et al., 2009). However, the chemical composition of berthierine in the Heimdal sandstone (this study) closely resembles the pore-filling berthierine in the Silurin Rose Hill Formation (Lu et al., 1994; Fig. 8). This chemical similarity may be explained by similar mineralogical educts, which are detrital Fe-Mg silicate grains (unspecified) in the Rose Hill Fm. (Lu et al., 1994) and glauconite in the Heimdal sandstone.

The exact chemical structure of berthierine as shown in Table 3 was calculated on the basis of 7 oxygens, using the procedure described by Brindley (1982). Since berthierine belongs to the serpentine group, it can be represented by the formula $(R^{2+}_a\ R^{3+}_b\square_c)(Si_{2-x}\ Al_x)\ O_5(OH)_4$ where R^{2+} and R^{3+} are cations (Fe^{2+}, Mg^{2+}, Fe^{3+}, Al^{3+}) occupying octahedral positions; represents possible vacant octahedral positions, and a+b+c=3 (Brindley, 1982). To calculate the structural formula, the total valence of cations in tetrahedral and octahedral positions was normalized to +14. This procedure ideally corresponds to an oxygen + water content $O_5(OH)_4$. Cations such as Na^+, K^+ and Ca^{2+} which cannot occupy octahedral positions are listed as small oxide percentages which can often be attributed to impurities. Tetrahedral positions not filled by Si^{4+} are filled by Al^{3+} cations. The formula of berthierine was calculated as presented in Table 2. At the tetrahedral sites, 20−27 mole% of Si are substituted by Al, and octahedral Al always exceeds tetrahedral Al. Compared with data summarized by Toth and Fritz (1997), berthierine in this study has a 5 mole%

less Fe content averaging at 1.645 mol%, whereas it has a 5 mole% higher Si content averaging at 1.541 mol%. The Si:Al molar ratio is higher than most of the reported berthierine data. Such high silica contents require a less Al substitution in the tetradedral layer (here: 18 mole% less Al in tetradedral layers).

5.5 *Organic geochemistry*

Oil alteration can be assessed by rations of branched against *n*-alkanes (Welte et al., 1982), since it is assumed that straight-chained *n*-alkanes like *n*-heptadecane (*n*-C_{17}) are more susceptible to be degraded than isoprenoids such as pristane (Wenger et al., 2002). A plot of pristane/*n*-C_{17} against phytane/*n*-C_{18} is the most commonly used evaluation to describe the extent of oil alteration in low to moderately biodegraded oil. The increasing values of pristane/*n*-C_{17} and phytane/*n*-C_{18} indicate an increasing extent of oil degradation from the gas cap and the oil leg towards the oil-water contact (Fig. 9). Thus, it appears that the highest oil degradation took place at the OWC which is the major reactive interface for oil degradation.

6. Discussion

The occurrence of berthierine was reported from various depositional environments highlighting the wide variability of possible crystal morphologies. In contrast to frequently reported berthierine ooids in non-oil bearing ironstones (Madon, 1992; Taylor and Curtis, 1995), berthierine in the Heimdal sandstone of the Siri oilfield mainly occurs as grain-coatings and pore-fillings. Moreover, berthierine in the Heimdal sandstone also grew in dissolved detrital glauconite grains and mica (Figs. 5a-d), or in form of mineralized net-like structures (Figs. 4e, 4f). Despite these association differences, the chemical berthierine uniformity in the Heimdal sandstone in figure 8 indicates that berthierine was formed under similar hydrogeochemical conditions.

6.1 In-situ berthierine formation

An detrital origin in form of sand deposition with berthierine as a detrital mineral can be ruled out, since berthierine coatings on detrital grains would have been completely or at least partly eroded from the grain surfaces due to sand transport over long distances (20−75 km) from the Stavanger platform area (Danielsen et al., 1995; Hamberg et al., 2005). In addition, berthierine also filled pores and is absent on grain-grain contacts (Figs. 2d, 2f, 2g and 5c), furthermore suggesting that berthierine formation must have taken place after compaction.

The euhedral habits of berthierine in oil-filled pores clearly indicate an in-situ formation. Berthierine crystals are frequently oriented vertically on grain surfaces (Figs. 4a, 4d), which is considered to be a characteristic of authigenic crystals (Coombs et al., 2000). Moreover, the in-situ precipitation of berthierine is also supported by its characteristic relationship to other minerals in the reservoir sandstone. Berthierine crystals co-occur in or on dissolved feldspar grains, suggesting that berthierine formed after or simultaneously with feldspar dissolution (Figs. 4b, 5f). Additionally, berthierine and quartz growth co-occurred, and the formation of berthierine may even postdate quartz growth since network-like berthierine networks cover microquartz overgrowth (Fig. 4f) and grain-coating berthierine was observed to cover quartz overgrowth (Figs. 2d, 4d). In addition, the interfaces between quartz overgrowths on quartz detrital grains often contain oil or small oil-water containing inclusions, indicating that quartz overgrowth started parallel with oil filling and continued. Thus, it can be inferred that berthierine formed parallel with and/or postdates oil filling. Berthierine occurs in dissolving glauconite grains and lamellae of mica/micaceous glauconite (Figs. 2c, 5c and 5d), but also replaced glauconite grains (Fig. 5a). Furthermore, berthierine is most abundant at the oil-water (OWC) which corresponds to relatively low amounts of glauconite (Table 1). These observations point to glauconite as a

precursor for berthierine in the Heimdal sandstone.

6.2 Berthierine formation

Precipitation of berthierine requires a depositional environment characterized by a massive supply of iron and reducing conditions (Curtis, 1985; Curtis and Spears, 1968). The influx of an external iron-rich fluid in an open system was considered to provide the iron for berthierine formation in porous sandstones (Lu et al., 1994; Stokkendal et al., 2009). However, Fu (2014) and Fu et al. (2015a) suggested that such fluid influxes are not controls for extensive berthierine formation as observed in the Siri field (5−15 vol.-% according to Stokkendal et al., 2009) due to the low concentrations of other aqueous species (e.g., Mg^{2+}, H_4SiO_4, and $Al(OH)_x^{+3-x}$) in such fluids.

Alternatively, berthierine in the Heimdal sandstone may have formed in a closed system in which the dissolution of glauconite and other minerals would have provided the required aqueous species composition needed for berthierine formation. Ferric iron dominates in glauconite compared to the dominance of ferrous iron in berthierine. Under anoxic conditions, the equilibration of glauconite with formation water may lead to the release of the following aqueous species into the formation water: K^+, Na^+, Mg^{2+}, Ca^{2+}, $SiO_{2(aq)}$, Al^{3+}, Fe^{2+}, and Fe^{3+} (Fig. 10). These released Fe^{3+} species are incapable of being removed from the formation water under anoxic and acidic conditions, and their relatively high activity prevents further glauconite dissolution. In contrast, Fe^{3+} species are transformed to Fe^{2+} species under reducing conditions. This leads to an oversaturation with regard to berthierine and enables its precipitation. Thus, dissolution of primary glauconite and following precipitation of berthierine needs reducing conditions and a sufficient supply with reducing agents. Oxidation of organic matter due to the iron reduction pathway during early diagenesis (prior to oil charging) may also lead to berthierine

formation (Taylor and Macquaker, 2011). However, the petrographic investigations showed that the sandstones of the Siri field are poor in sedimentary organic matter. Organoclasts such as lignite, alginite, etc., were not observed in the Heimdal sandstone. Thus, it can be inferred that only small amounts of berthierine formed by iron reduction during early diagenesis due to the lack of reducing agents such as sedimentary particulate organic matter.

Based on the above presented considerations, an alternative explanation for the occurrence of berthierine in the Heimdal sandstone is presented which relates it to oil degradation in the reservoir. The oil which originally was or which today is in the reservoir can act as reductant for Fe^{3+} in glauconite into Fe^{2+}. Due to this reduction, glauconite dissolution proceeded, causing hydrogeochemical conditions leading to the precipitation of berthierine (Fig. 10). Evidence for this scenario can be clearly observed in figure 2e.

6.3 Organic-inorganic interactions due to oil degradation: the control of berthierine formation

Anaerobic oil degradation is a well-known process, and controlled by a maximum temperature of around 80 °C (Wilhelms et al., 2001). Oil degradation takes place near the oil-water contact (Larter et al., 2003), but also occurs throughout the hydrocarbon column in water-wet reservoirs, especially in the irreducible water film (e.g., Wenger et al., 2002). The products of anaerobic hydrocarbon degradation (oxidation of, e.g., aqueous *n*-alkanes) are methane, carbon dioxide, hydrogen, and acetic acid which are being released into the pore water (Seewald, 2003; Fig. 10). A consequence of these processes is that reactive minerals (glauconite and feldspars) may dissolve under the changed hydrogeochemical conditions, and that minerals such as berthierine may newly form (Fig. 10).

6.3.1 Oil degradation

The today´s produced oil in the Siri field has API gravities of more than 35°. However, the first oil filling might have also undergone degradation when the reservoir was buried to approximately 1,000m depth (Hamberg et al., 2005; Ohm et al., 2006). Tectonic movements led to leakage and a second filling phase later. In addition, the present-day gas in the Siri field, which is dissolved in oil, is characterized by δ^{13}C-methane values of around −50‰, by δ^{13}C-ethane values of around −33‰, and by low gas wetness values of less than 10 (Ohm et al., 2006). Such data also indicate a slight degradation level of the present-day oil and that biogenic methane gas contributions due to oil degradation are assumed for the investigated Siri fields.

A striking feature pointing to oil degradation are the berthierine net-like structures (berthierine type 1, subtype IV; Figs. 4e, 4f) which resemble mineralized oil-water emulsions (e.g., Mandal et al., 2010; Sullivan and Kilpatrick, 2002). The occurrence of oil-water emulsions is known from oil-water contacts where they are stabilized, e.g., by asphaltenes (which are enriched in degraded oils). In general, they occur in reservoirs with API gravities lower than 25° and temperatures lower than 66 °C, but also occur in tar mats in oil reservoirs (Wilhelms and Larter, 1994a, 1994b).

Evidence for a potential formation of the mineralized oil-water emulsions due to oil degradation is a higher degradation rank of the investigated oil in the Heimdal sandstone. Increased nitrogen contents of oil in an electron energy loss spectroscopy (EELS) spectrum (insert in Fig. 6g) may indicate oil alteration. Since crude oil contains less than 1% nitrogen, the enrichment of heterocyclic aromatic compounds containing nitrogen, sulfur, or oxygen (NSO compounds) reflects oil alteration processes (Curiale et al., 1983). Oil alteration is also assessed by plotting pristane/*n*-C_{17} versus phytane/*n*-C_{18} (Fig. 9). Samples from the OWC show a relatively high extent of oil degradation indicated by relatively higher values of Pr/*n*-C_{17} and Ph/*n*-C_{18} at the OWC compared with samples from the gas cap and the oil leg (Fig. 9). In these

intervals (together with the oil leg), most of the authigenic berthierine occurs (Table. 1), and supports our observations about a genetic relation between oil degradation and berthierine formation in the Heimdal sandstone in the Siri field.

6.3.2 Organic-inorganic interactions trigged by oil degradation leading to berthierine formation

Our working hypothesis is that berthierine formation in the Siri field is due to glauconite dissolution within a close system due to gas-fluid-rock interactions driven by oil degradation at oil-water contacts but also at oil-water interfaces in the oil-filled reservoir (Fig. 10). The water saturation of the Heimdal sandstone is as high as 30−40% in the oil leg and the Heimdal sandstone is thus water-wet. In water-wet reservoirs, extensive oil-water interfaces may be still maintained by water-coated mineral surfaces when aqueous pore fluids are displaced by hydrocarbons (Karlsen et al., 1993; Treiber et al., 1992). At such oil-water interfaces, which thus also exist in the oil leg, the important reaction named "hydrolytic disproportionation" (Seewald, 2003) may take place during which oil degradation products (methane, carbon dioxide, hydrogen, and acetate) are being released into the pore water.

Consequently, minerals which are thermodynamically unstable at specific hydrogeochemical conditions, e.g., glauconite and feldspars, firstly dissolve and release K^+, Na^+, Mg^{2+}, Ca^{2+}, $SiO_{2(aq)}$, Al^{3+}, Fe^{2+}, and Fe^{3+} species into the formation water. In addition, with the supply of reducing agents from oil degradation, such as CH_4, H_2, and CH_3COOH (acetic acid) generated at oil-water interfaces, the reduction of Fe^{3+} (mainly released from glauconite) to Fe^{2+} may take place (Fig. 10) and leads to berthierine formation when its saturation is achieved. Berthierine formation may be favored close to iron-bearing minerals (e.g., glauconite) due to the short transportation distance of ions (Bjørlykke and Jahren, 2012). Potentially co-existing reactions

may lead to quartz overgrowth (Fig. 10; Fu, 2014; Fu et al., 2015a).

6.4. Implications

Fluid-rock interactions may alter the original composition of petroleum fluids trapped in petroleum reservoirs, but consequently also the aqueous phase and the mineral matrix. A threshold of around 80°C is discussed for such "degradation" processes (Wilhelms et al., 2001), but hydrolytic disproportionation may continue at higher temperatures and can lead to further degradation of petroleum compounds (Seewald, 2003). However, quantitative approaches about the overall consequences of such complex organic-inorganic interactions are still rare, and the significance of such processes is underestimated.

The conversion of mineralizable organic components is an overall control for severe changes of the mineral matrix in sedimentary basins. Mineralizable organic matter occurs from shallow to great depth, and is thus ubiquitously available for coupled organic-inorganic interactions. The actual processes take place in aqueous phase which mainly occur in residual water in pores and in the irreducible water film around mineral grains. By far the most significant interface for such processes is the OWC in oil fields. The presented data about the Siri field in the Danish North Sea highlight the possible conversion of glauconite into berthierine at such interfaces, but also point to the fact that altered petroleum residues are involved in this complex web of interconnected processes. However, the presented results raise new questions. How much of the petroleum needs to be converted to cause the observed present mineral composition of the Heimdal reservoir in the Siri field? Is the observed precipitation of berthierine an indicator of an intense oil degradation? The more observations, the more questions. Quantitative approaches are needed to answer questions about the "where", "when", and "how much" of complex rock-fluid-gas interactions. Such new conceptual approaches have strong implications for the assessment of

reservoir properties and possible production measures. Moreover, quantitative hydrogeochemical modelling may help to unravel the diagenetic histories of sedimentary sequences in basins which host organic-rich intervals (such as oil-bearing reservoirs, black shales or coal measures) which may release products like methane, carbon dioxide, etc. during diagenetic process. In consequence, mass balancing will highlight the significance of such organic compounds for the diagenetic history of sedimentary basins, and will not exclusively rely on "classical" diagenetic models.

7. Conclusions

1. Berthierine is the only authigenic Fe-rich clay mineral which occurs in the Heimdal sandstone revealed by applying a combination of various analytical methods. It appears as grain-coating, pore-filling and also as blade-like crystals in glauconite, mica and siderite concretions. Berthierine predominantly occurs at the oil-water contact, and shows similarly chemical composition independent on type. Its relationship with other minerals indicates that it formed in-situ and after oil emplacement.

2. Berthierine frequently grows in glauconite and partly replaces glauconite grains. Its predominant abundance at the OWC, where the lowest amounts of glauconite prevail, points to glauconite as the precursor for berthierine. Since berthierine formation requires sufficient organic matter, which is not abundant in the Heimdal sandstones prior to oil charging, the oil filling and its degradation products in the Heimdal sandstones could have created suitable conditions for berthierine formation.

3. The Siri field shows a slightly higher degree of oil degradation at the oil-water contacts by higher values of Pr/*n*-C_{17} and Ph/*n*-C_{18}. The possible concept for the formation of berthierine could be that oil degradation products (CH_4, H_2, CO_2, and CH_3COOH) dissolved in formation

water, lowered pH, and, consequently, led to dissolution of thermodynamically instable minerals (such as glauconite, mica and feldspar) and to the precipitation of thermodynamically stable minerals, e.g., quartz overgrowth, siderite and berthierine.

4. Unlike previous hypotheses to explain the origin of berthierine in (Boyd et al, 2004; Hornibrook and Longstaffe, 1996; Lu et al., 1994), the presented results offer a new interpretation concept of berthierine formation: oil emplacement and following oil degradation may have caused a web of interconnected processes during which berthierine formed in oil-filled zones, especially in water-wet reservoir units.

Acknowledgements

Funding of Nana Mu was provided by the Chinese Scholarship Council (CSC). The authors would like to thank DONG Energy and the Geological Survey of Denmark and Greenland for supporting the study, and for access to core samples and data. The original manuscript was improved following reviews by Lynda Williams. Professor Carlos Rossi Nieto and an anonymous reviewer are thanked for their constructive reviews that helped to improve the manuscript.

References

Bailey, S.W., 1988. Odinite, a new dioctahedral-trioctahedral Fe^{3+}-rich l:l clay mineral. Clay Miner. 23, 237–247.

Bhattacharyya, D.P., 1983. Origin of berthierine in ironstones. Clays Clay Miner. 31, 173–182.

Bjørlykke, K., Jahren, J., 2012. Open or closed geochemical systems during diagenesis in sedimentary basins: Constraints on mass transfer during diagenesis and the prediction of porosity in sandstone and carbonate reservoirs. Am. Assoc. Pet. Geol. Bull. 96, 2193–2214.

Boyd, G.A., Wallace, M.W., Holdgate, G.R., Gallagher, S.J., 2004. Marine clays and porosity

evolution in Nullawarre Greenland, Otway Basin, southeastern Australia, in: PESA Eastern Australasian Basins Symposium II held in Adelaide, 20–22 September, 2004.

Brindley, G.W., 1982. Chemical compositions of berthierines−A review. Clays Clay Miner. 30, 153–155.

Coombs, D.S., Zhao, G., Peacor, D.R, 2000. Manganoan berthierine, Meyers Pass, New Zealand: occurrence in the prehnite-pumpellyite facies. Mineral. Mag. 64, 1037–1046.

Curiale, J.A., Harrison, W.E., Smith, G., 1983. Sterane distribution of solid bitumen pyrolyzates. Changes with biodegradation of crude oil in the Ouachita Mountains, Oklahoma. Geochim. Cosmochim. Acta 47, 517–523.

Curtis, C.D., 1985. Clay mineral precipitation and transformation during burial diagenesis. Philos. Trans. R. Soc. London, Ser. A, Mathmatical Phys. Sci. A315, 91–105.

Curtis, C.D., Spears, D.A., 1968. The formation of sedimentary iron minerals. Econ. Geol. 24, 257–270.

Damyanov, Z., Vassileva, M., 2001. Authigenic phyllosilicates in the Middle Triassic Kremikovtsi sedimentary exhalative siderite iron formation, Western Balkan, Bulgaria. Clays Clay Miner. 49, 559–585.

Danielsen, M., Clausen, O.R., Michelsen, O., 1995. Stratigraphic correlation of late Paleocene sand deposits in the Søgne Basin area of the Danish and Norwegian central North Sea. Terra Nov. 7, 516–527.

Deer, W.A., Howie, R.A., Zussman, J., 1992. An introduction to the rock forming minerals, 2nd ed., Longman, London, pp. 696.

Fritz, S.J, Toth, T.A, 1997. An Fe-berthierine from a Cretaceous laterite: Part II. Estimation of Eh, pH and pCO_2 conditions of formation. Clays Clay Miner. 45, 580–586.

Fu, Y., 2014. Development and application of numerical modeling for evaluating and predicting

hydrogeochemical processes temporally and spatially evolving in petroleum reservoirs: Case studies: Miller oilfield (UK North Sea) and Siri oilfield (Danish North Sea). Ph.D. thesis, Clausthal University of Technology, 76–83.

Fu, Y., van Berk, W., Schulz, H.-M., Mu, N., 2015a. Berthierine formation in reservoir rocks from the Siri oilfield (Danish North Sea) as result of fluid-rock interactions: Part II. Deciphering organic-inorganic processes by hydrogeochemical modeling. Mar. Pet. Geol., http://dx.doi.org/10.1016/j.marpetgeo.2015.01.007

Fu, Y., van Berk, W., Schulz, H.-M., Mu, N., 2015b. Berthierine formation in reservoir rocks from the Siri oilfield (Danish North Sea) as result of fluid-rock interactions: Part III. Deciphering mineral stability and CO2-sequestering capacity of glauconitic sandstones. Mar. Pet. Geol., http://dx.doi.org/10.1016/j.marpetgeo.2015.01.008

Hamberg, L., Dam, G., Wilhelmson, C., Ottesen, T., 2005. Palaeocene deep-marine sandstone plays in the Siri Canyon, offshore Denmark-southern Norway, in Doré, A.G., Vining, B.A. (Eds.), Petroleum Geology: North-West Europe and Global Perspectives, Proceedings of the 6th Petroleum Geology Conference. Geological Society of London, pp. 1185–1198.

Harder, H., 1978. Synthesis of iron layer silicate minerals under natural conditions. Clays Clay Miner. 26, 65–72.

Harder, H., 1989. Mineral genesis in ironstones: a model based upon laboratory experiments and petrographic observations, in: Yong, T.P., Taylor, W.E.G. (Eds.), Phanerozoic Ironstones 46, Geological Society, London, Special Publication, pp. 9–18.

Hornibrook, E.R.C, Longstaffe, F.J., 1996. Berthierine from the lower cretaceous clearwater formation, Alberta, Canada. Clays Clay Miner. 44, 1–21.

Huggett, J.M., Hesselbo, S.P., 2003. Low oxygen levels in earliest Triassic soils: Comment and Reply: COMMENT. Geology 31, e20–e20.

Huggett, J.M., Gale, A.S., 2002. Petrology and environmental significance of iron-rich clays in the Middle Eocene of NE Texas, in: Bolder Clays: Clay Minerals Society 39th Annual Meeting Program and Abstracts.

Huuse, M., 1999. Detailed morphology of the top Chalk surface in the eastern Danish North Sea. Pet. Geosci. 5, 303–314.

Iijima, A., Matsumoto, R., 1982. Berthierine and chamosite in coal measures of Japan. Clays Clay Miner. 30, 264–274.

Karlsen, D.A., Nedkvitne, T., Larter, S.R., Bjørlykke, K., 1993. Hydrocarbon composition of authigenic inclusions: Application to elucidation of petroleum reservoir filling history. Geochim. Cosmochim. Acta 57, 3641–3659.

Kodama, H., Foscolos, A., 1981. Occurrence of berthierine in Canadian Arctic desert soil. Can. Mineral. 19, 279–283.

Larter, S., Wilhelms, A., Head, I., Koopmans, M., Aplin, A., Di Primio, R., Zwach, C., Erdmann, M., Telnaes, N., 2003. The controls on the composition of biodegraded oils in the deep subsurface—part 1: biodegradation rates in petroleum reservoirs. Org. Geochem. 34, 601–613.

Lu, G., .McCabe, C., Henry, D.J., Schedl, S., 1994. Origin of hematite carrying a Late Paleozoic remagnetization in a quartz sandstone bed from the Silurian Rose Hill Formation, Virginia, USA. Earth Planet. Sci. Lett. 126, 235–246.

Madon, M.B.H., 1992. Depositional setting and origin of berthierine oolitic ironstones in the lower Miocene Terengganu Shale, Tenggol Arch, offshore peninsular Malaysia. J. Sediment. Res. 62, 899–916.

Mandal, A., Samanta, A., Bera, A., Ojha, K., 2010. Characterization of oil-water emulsion and its use in enhanced oil recovery. Ind. Eng. Chem. Res. 49, 12756–12761.

Maynard, J.B., 1986. Geochemistry of oolitic iron ores, an electron microprobe study. Econ. Geol. 81, 1473–1483.

Odin, G.S., 1990. Clay mineral formation at the continent-ocean boundary: the Verdine facies. Clay Miner. 25, 477–483.

Ohm, S.E., Karlsen, D.A., Roberts, A., Johannessen, E., Høiland, O., 2006. The Paleocene sandy Siri Fairway: An efficient "pipeline" draining the prolific Central Graben? J. Pet. Geol. 29, 53–82.

Petrovich, R., 2001. Mechanisms of fossilization of the soft-bodied and lightly armored faunas of the Burgess Shale and of some other classical localities. Am. J. Sci. 301, 683–726.

Poulsen, M.L.K., Friis, H., Svendsen, J.B., Jensen, C.B., Bruhn, R., 2007. The application of bulk geochemistry to reveal heavy mineral sorting and flow units in thick massive gravity flow deposits, Siri Canyon Palaeocene Sandstones, Danish North Sea, in: Heavy Minerals in Use 58, Developments in Sedimentology, Elsevier, Amsterdam, pp. 1099–1121.

Rivard, C., Pelletier, M., Michau, N., Razafitianamaharavo, A., Bihannic I., Abelmoula, M., Ghanbaja, J., Villieras, F., 2013. Berthierine-like mineral formation and stability during the interaction of kaolinite with metallic iron at 90 C under anoxic and oxic conditions. Am. Mineral. 98, 163–180.

Rivas-Sanchez, M.L., Alva-Valdivia, L.M. Arenas-Alatorre, J., Urrutia-Fucugauchi, M., Ruiz-Sandoval, M., Ramos-Molina, M.A., 2006. Berthierine and chamosite hydrothermal: genetic guides in the Pena Colorada magnetite-bearing ore deposit, Mexico. Earth Planets Space 58, 1389–1400.

Rohrlich, V., Price, N.B., Calvert, S.E., 1969. Chamosite in recent sediments of Loch Etive, Scotland. J. Sediment. Petrol. 39, 624–631.

Ruotsala, A. P., Pfluger, C. E., Garnett, M., 1964. Iron-rich serpentine and chamosite from Ely,

Minnesota. Am. Mineral. 49, 993–1001.

Sánchez-Navas, A., Martín-Algarra, A., Eder, V, Reddy, B.J., Nieto, F, Z, Zanin, Y.N., 2008. Color, mineralogy and composition of Upper Jurassic West Siberian glauconite: useful indicators of paleoenvironment. Can. Mineral. 46, 1249–1268.

Seewald, J.S., 2003. Organic-inorganic interactions in petroleum-producing sedimentary basins. Nature 426, 327–333.

Sheldon, N.D., Retallack, G.J., 2002. Low oxygen levels in earliest Triassic soils. Geology 30, 919.

Slack, J.F., Jiang, W.T., Peacor, D.R., Okita, P.M., 1992. Hydrothermal and metamorphic berthierine from the Kidd Creek volcanogenic massive sulfide deposit, Timmins, Ontario. Can. Mineral. 30, 1127–1142.

Stokkendal, J., Friis, H., Svendsen, J.B., Poulsen, M.L.K., Hamberg, L., 2009. Predictive permeability variations in a Hermod sand reservoir, Stine Segments, Siri Field, Danish North Sea. Mar. Pet. Geol. 26, 397–415.

Sullivan, A.P., Kilpatrick, P.K., 2002. The effects of inorganic solid particles on water and crude oil emulsion stability. Ind. Eng. Chem. Res. 41, 3389–3404.

Taylor, K., 1990. Berthierine from the non-marine Wealden (Early Cretaceous) sediments of south-east England. Clay Miner. 25, 391–399.

Taylor, K.G., Curtis, C.D., 1995. Stability and facies association of early diagnetic mineral assemblages: an example from a Jurassic ironstone-mudstone succession, U.K. J. Sediment. Res. A65, 358–368.

Taylor, K.G., Macquaker, J.H.S., 2011. Iron minerals in marine sediments record chemical environments. Elements 7, 113–118.

Toth, T., Fritz, S., 1997. An Fe-berthierine from a cretaceous laterite: Part I. Characterization.

Clays Clay Miner. 45, 564–579.

Treiber, L.E., Archer, D. L., Owens, W.W., 1992. Laboratory evaluation of the wettability of 55 oil producing reservoirs. Soc. Pet. Eng. 12, 531–540.

Van Houten, F.B., Purucker, M.E., 1984. Glauconitic peloids and chamositic ooids-favorable factors, constraints, and problems. Earth Sci. Rev. 20, 211–243.

Welte, D.H., Kratochvil, H., Rullkötter, J., Ladwein, H., Schaefer, R.G., 1982. Organic geochemistry of crude oils from the Vienna Basin and an assessment of their origin. Chem. Geol. 35, 33-68.

Wenger, L.M., Davis, C.L., Isaksen, G.H., Upstream, E., 2002. Multiple controls on petroleum biodegradation and impact on oil quality, in: 2002 SPE Reservoir Evaluation & Engineering. pp. 375–383.

Wilhelms, A., Larter, S.R., 1994a. Origin of tar mats in petroleum reservoirs. Part I: introduction and case studies. Mar. Pet. Geol. 11, 418–441.

Wilhelms, A., Larter, S.R., 1994b. Origin of tar mats in petroleum reservoirs . Part II: formation mechanisms for tar mats. Mar. Pet. Geol. 11, 442–456.

Wilhelms, A., Larter, S. R., Head, I., Farrimond, P., Di-Primio, R., Zwach, C., 2001. Biodegradation of oil in uplifted basins prevented by deep-burial sterilization. Nature 411, 1034–1037.

Wirth, R., 2004. Focused ion beam (FIB): a novel technology for advanced application of micro- and nanoanalysis in geosciences and applied mineralogy. Eur. J. Mineral. 16, 863–876.

Wirth, R., 2009. Focused Ion Beam (FIB) combined with SEM and TEM: Advanced analytical tools for studies of chemical composition, microstructure and crystal structure in geomaterials on a nanometre scale. Chem. Geol. 261, 217–229.

Wise, M.A., 2007. Crystallization of “pocket” berthierine from the pulsifer granitic pegmatite,

Poland, Maine, USA. Clays Clay Miner. 55, 583–592.

Worden, R., Morad, S., 2003. Clay minerals in sandstones: controls on formation, distribution and evolution, in: Worden, R. H., Morad, S. (Eds.), Clay Mineral Cements in Sandstones, 34, International Association of Sedimentologists Special Publication, pp. 3–41.

Tables

Table 1. Point counted composition of samples from well Siri-2.

Depth (m)	Zone	Detrital (%)				Authigenic (%)					Porosity %	Sum %
		Quartz	Feldspar	Glauconite	Mica	Quartz overgrowth	Berthierine	Kaolinite	Siderite	Calcite		
2102.80	Gas cap	33.1	14.97	48.07	0.35	4.91	2.57	1.52	0.12	2.11	19.53	100
2104.40	Gas cap	26.32	17.19	43.51	2.11	3.68	2.63	4.39	—	0.18	13.68	100
2108.40	Oil leg	26.32	20.18	46.49	1.58	2.98	2.98	1.58	0.88	0.35	11.58	100
2110.60	Oil leg	34.74	13.68	48.42	2.28	4.56	1.93	2.11	0.18	—	16.67	100
2113.15	Oil leg	23.86	17.02	40.88	1.58	4.04	4.39	2.98	7.72	—	13.51	100
2116.30	OWC	24.56	14.56	39.12	0.18	2.98	7.72	0	0.35	36.14	—	100
2116.90	OWC	25.26	15.61	40.88	2.46	3.86	3.86	2.81	2.81	9.3	11.05	100
2136.55	Water leg	32.11	17.37	49.47	1.93	5.96	1.93	2.98	1.75	—	12.98	100

— indicates absence.

Table 2. Occurrence of five different berthierine types in the Heimdal sandstone of Siri field

Locations	Type 1				Type 2	Type 3	Type 4	Type 5
	Subtype I	Subtype II	Subtype III	Subtype IV				
Gas cap	x	x		x	x	x	xx	
Oil leg	xx	x	x	xxx	x	xx	xxx	xx
OWC	xx	x		xxx	xx	xxx	xxx	x
Water leg	x	x	x	x	x	x	x	

Such observed occurrence is a semi-quantitative presentation based on microscopic appearance. Occurrence: x = few; xx = mean; xxx = frequent.

Table 3. Representative microprobe analyses (wt.-%) and structural formulae of berthierine crystals in one core sample from the oil leg and one sample from the water leg.

	Oil leg						Water leg		
	1	2	3	4	5	6	7	8	9
SiO_2	30.28	30.36	28.51	26.38	27.65	27.88	29.42	29.21	27.6
FeO	35.48	37.38	37.19	38.19	36.75	37.31	35.19	34.14	36.81
Al_2O_3	21.95	22.2	21.54	21.74	21.03	21.28	19.8	19.49	20.42
MgO	3.7	3.67	3.08	3.25	3.62	3.59	4.66	5.24	4.09
MnO	0.06	0.09	0.08	0.07	0.1	0.06	0.07	0.1	0.09
CaO	0.44	0.37	0.36	0.34	0.22	0.11	0.29	0.69	0.24
Na_2O	0.14	0.26	0.1	0.16	0.35	0.32	0.35	0.26	0.32
K_2O	0.23	0.19	0.35	0.11	0.05	0.07	0.86	1.12	0.53
Total	92.28	94.52	91.2	90.24	89.77	90.62	90.63	90.26	90.1
Si^{4+}	1.587	1.566	1.538	1.455	1.517	1.516	1.588	1.582	1.516
Fe^{2+}	1.555	1.613	1.677	1.762	1.687	1.697	1.588	1.546	1.691
Al(tet)	0.41	0.43	0.458	0.541	0.478	0.481	0.409	0.413	0.48
Al(oct)	0.947	0.92	0.911	0.873	0.883	0.884	0.851	0.831	0.843
Mg^{2+}	0.289	0.282	0.247	0.267	0.296	0.291	0.375	0.423	0.335
Mn^{2+}	0.003	0.004	0.004	0.003	0.005	0.003	0.003	0.005	0.004
Ca^{2+}	0.025	0.021	0.021	0.02	0.013	0.007	0.017	0.04	0.014
Na^{+}	0.014	0.026	0.011	0.017	0.038	0.033	0.037	0.028	0.034
K^{+}	0.016	0.013	0.024	0.007	0.003	0.005	0.059	0.078	0.037
□	0.208	0.184	0.164	0.098	0.135	0.128	0.186	0.2	0.13
Fe/(Fe+Mg)	0.84	0.85	0.87	0.87	0.85	0.85	0.81	0.79	0.83
Mg/Fe	0.19	0.18	0.15	0.15	0.18	0.17	0.24	0.27	0.2
Al/Si	0.85	0.86	0.89	0.97	0.9	0.9	0.79	0.79	0.87

Total Fe as FeO. The formulae were calculated on the basis of 7 oxygens. Oxides are in weight percentage; ions are in mole percentage.

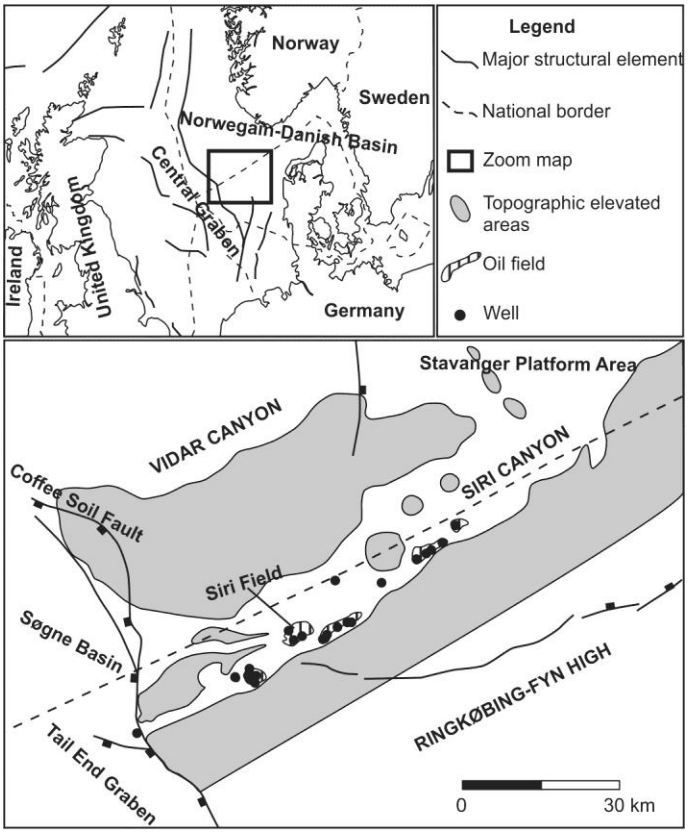

Figure 1. Location map of the study area in the Danish North Sea sector and depositional environment during the Paleocene (modified after Hamberg et al., 2005).

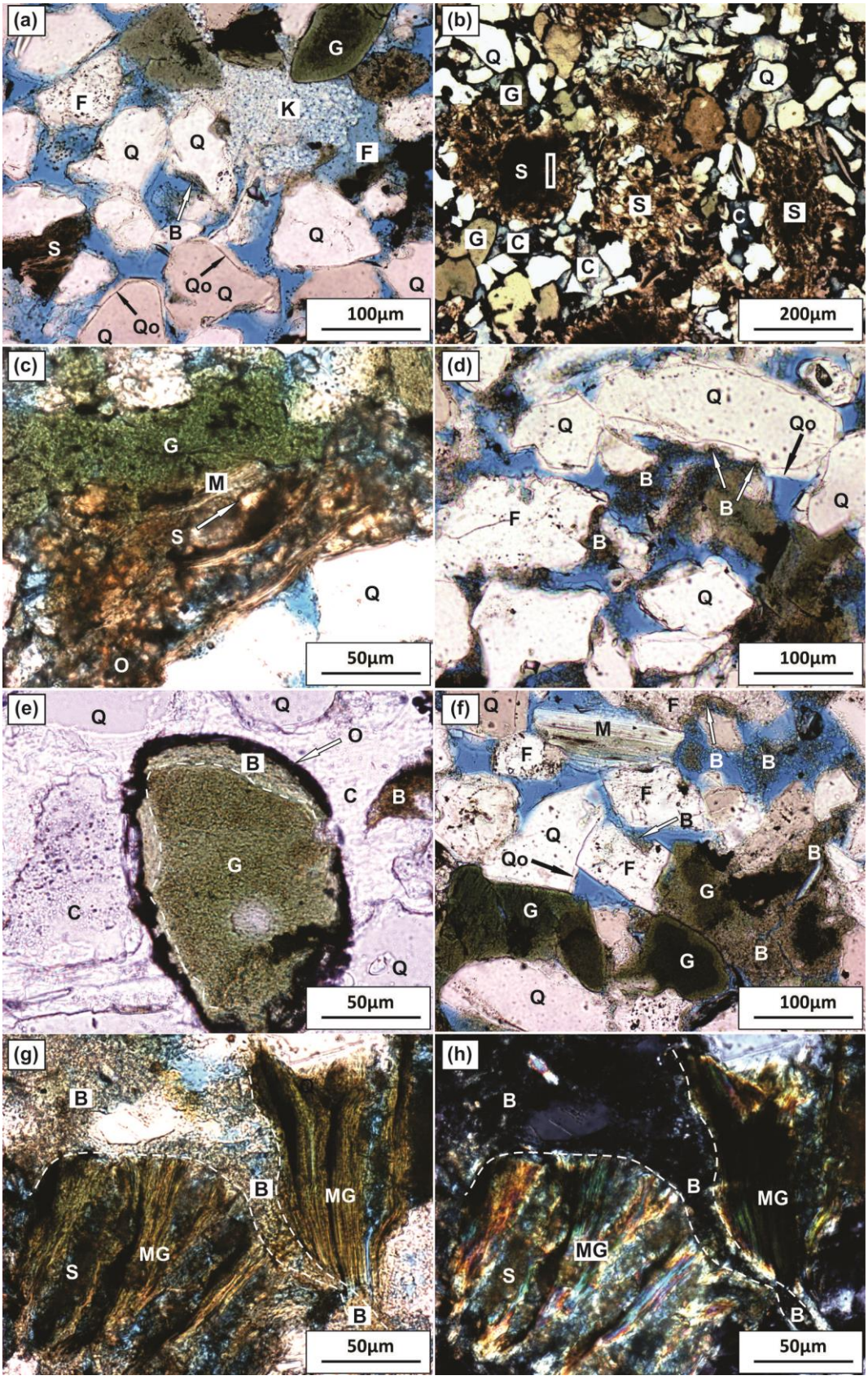

Figure 2. Thin section microphotographs (// nicols) of core samples from the Paleocene

Heimdal Member of the Lista Formation in the Siri field. (a) General mineralogical composition of the Heimdal sandstone, Well Siri-2, oil leg. (b) Siderite clusters and calcite cements filling the pore space; the area marked by a red rectangle was investigated by TEM (results in Figure 8a), Well Siri-2, oil leg. (c) Siderite growing between lamella of bitumen stained mica, Well Siri-2, oil leg. (d) Pore-filling berthierine in pores. Berthierine also occurs as grain coating together with quartz overgrowth and also partly on quartz overgrowth indicated by red arrows, Well Siri-1, water leg. (e) Glauconite grain with lighter green berthierine coating surrounded by a black ribbon of residual bitumen, Well Siri-1, OWC (Fu, 2014). (f) Brownish berthierine as pore-filling clay in open pore space and also as grain-coating on dissolved feldspar indicated by red arrows. Note that brownish berthierine in the lower right corner replaces dissolved green glauconite, Well Siri-1, water leg. (g) Brown-green berthierine filling in pore space close to micaceous glauconite which contains siderite in lamellas. Note that the interface of berthierine and micaceous glauconite is transitional, Well Siri-1, oil leg. (h) g under crossed nicols. Q: quartz; Qo: quartz overgrowth; G: glauconite; MG: micaceous glauconite; M: mica; K: kaolinite; F: feldspar; S: siderite; C: calcite; B: berthierine; O: residual oil; pores in blue.

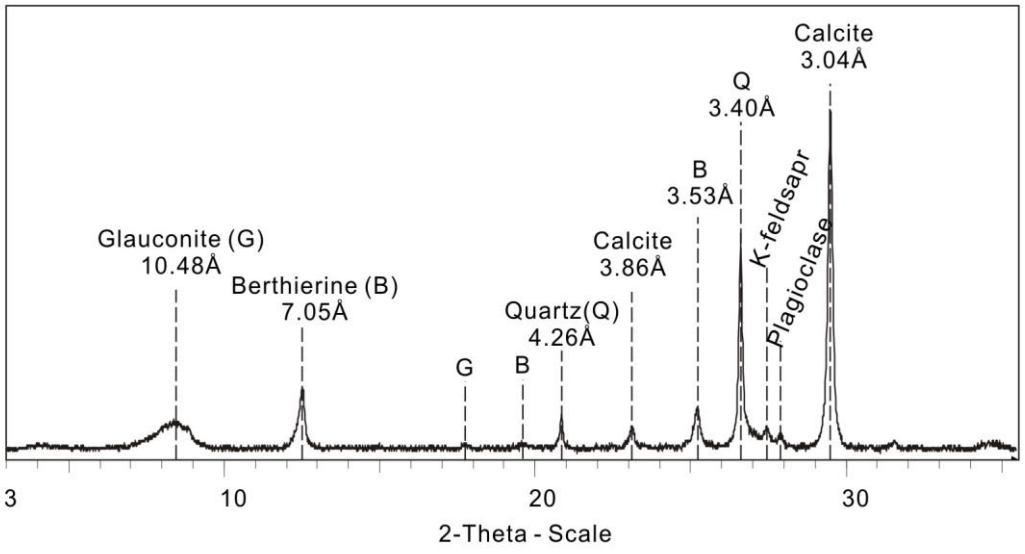

Figure 3. Representative XRD pattern (orientated, air-dried) of berthierine in the Heimdal sandstone, Well Siri-2, OWC. Note that only 0.7nm peak is present and there is no 1.4nm peak, indicating the exclusive presence of berthierine rather than chlorite in the Heimdal sandstone.

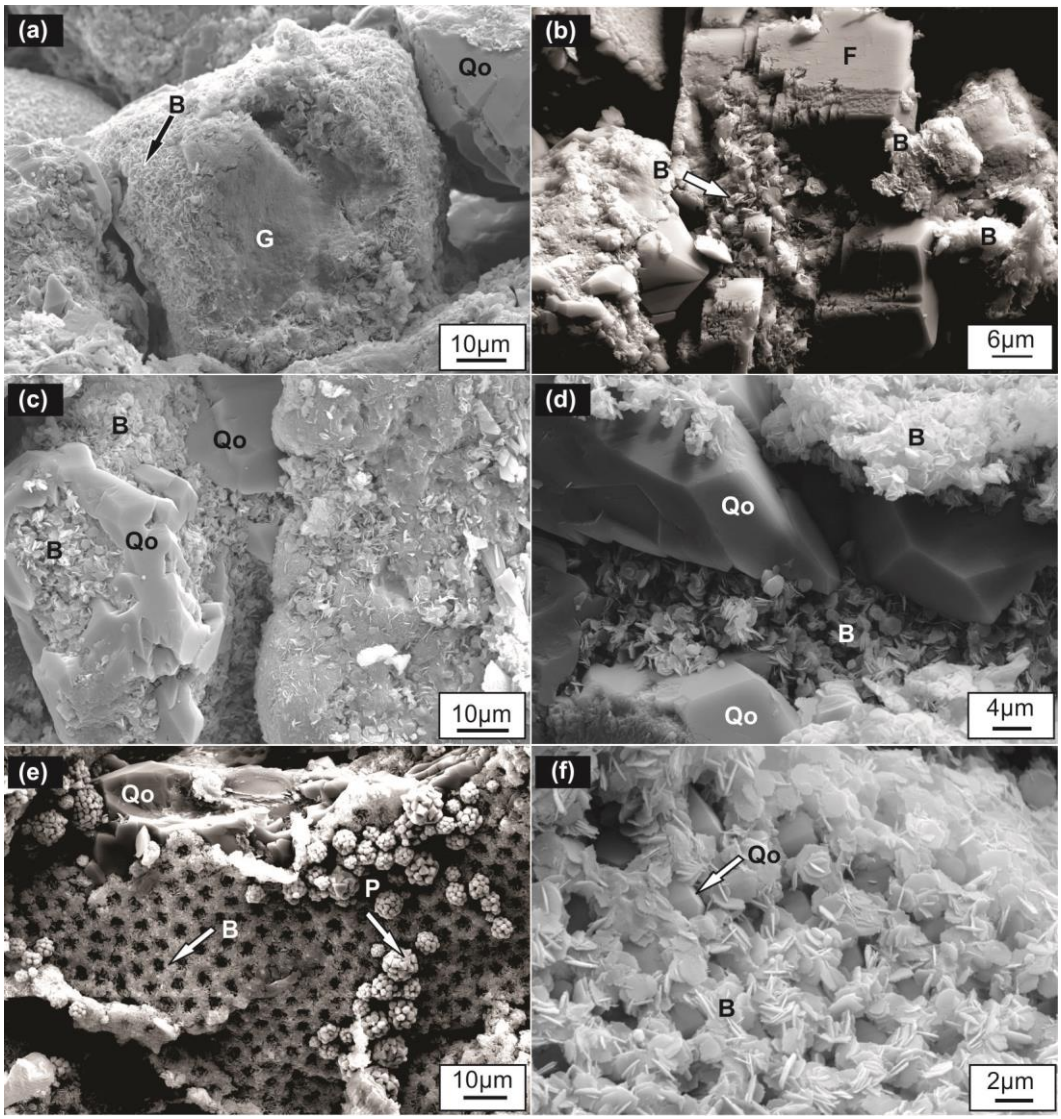

Figure 4. SEM micrographs of berthierine type 1. (a) Subtype I: as coating on a glauconite grain, Well Siri-2, oil leg. (b) Subtype II: berthierine coating on dissolved feldspar. (c) Subtype III: berthierine coating surrounded by quartz overgrowth, Well Siri-2, oil leg; (d) Berthierine coating on quartz overgrowth, Well Siri-2, OWC. (e) Subtype IV: berthierine net with attached pyrite framboids, Well Siri-1, oil leg (Fu, 2014); (f)

Berthierine net coating microquartz, Well Siri-2, OWC. B: berthierine; G: glauconite; Q: quartz; Qo: microquartz; M: mica; S: siderite; P: pyrite; C: calcite cement.

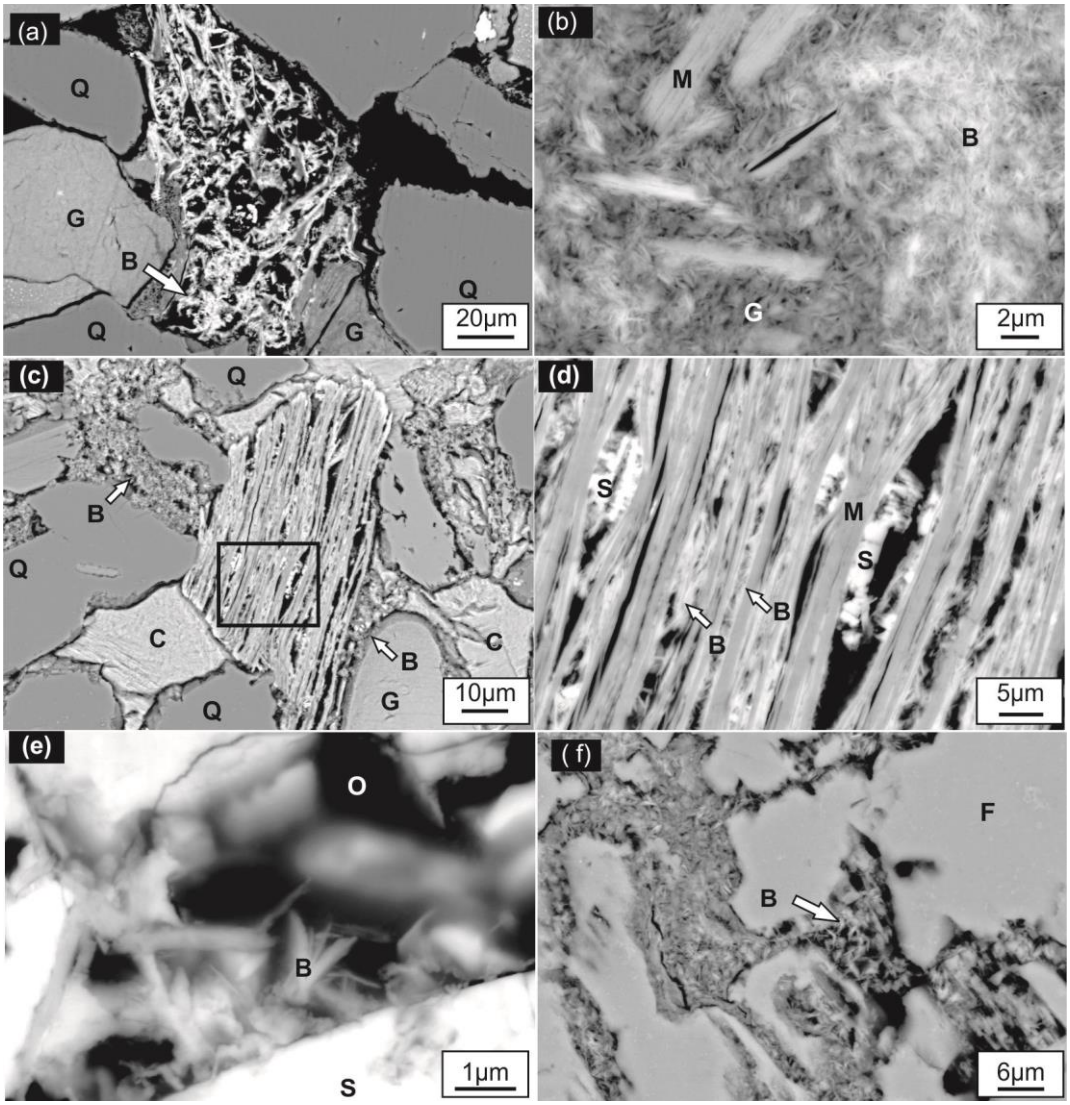

Figure 5. BSE images of berthierine types. (a) Type 3: berthierine (bright area) growing in strongly dissolved glauconite, Well Siri-2, oil leg; (b) Growth of berthierine crystals (bright areas) together with muscovite in transforming glauconite, Well Siri-2, OWC. (c) Type 2: pore filling berthierine (the upper left corner) cemented by calcite. The glauconite grain in the lower right corner is covered by berthierine type 1 (white arrow), Well Siri-2, OWC. (d) Type 4: as elongated crystals together with newly formed siderite between lamellae of mica transformed from glauconite. High resolution image of the rectangle area in c, Siri-2, OWC. (e) Type 5: berthierine in siderite concretions, Well

Siri-2, Oil leg. (f) Type 1, Subtype II: berthierine growing in dissolved feldspar, Well Siri-2, oil leg. B: berthierine; G: glauconite; Q: quartz; M: mica; C: calcite cement; S: siderite; O: residual oil; F: feldspar.

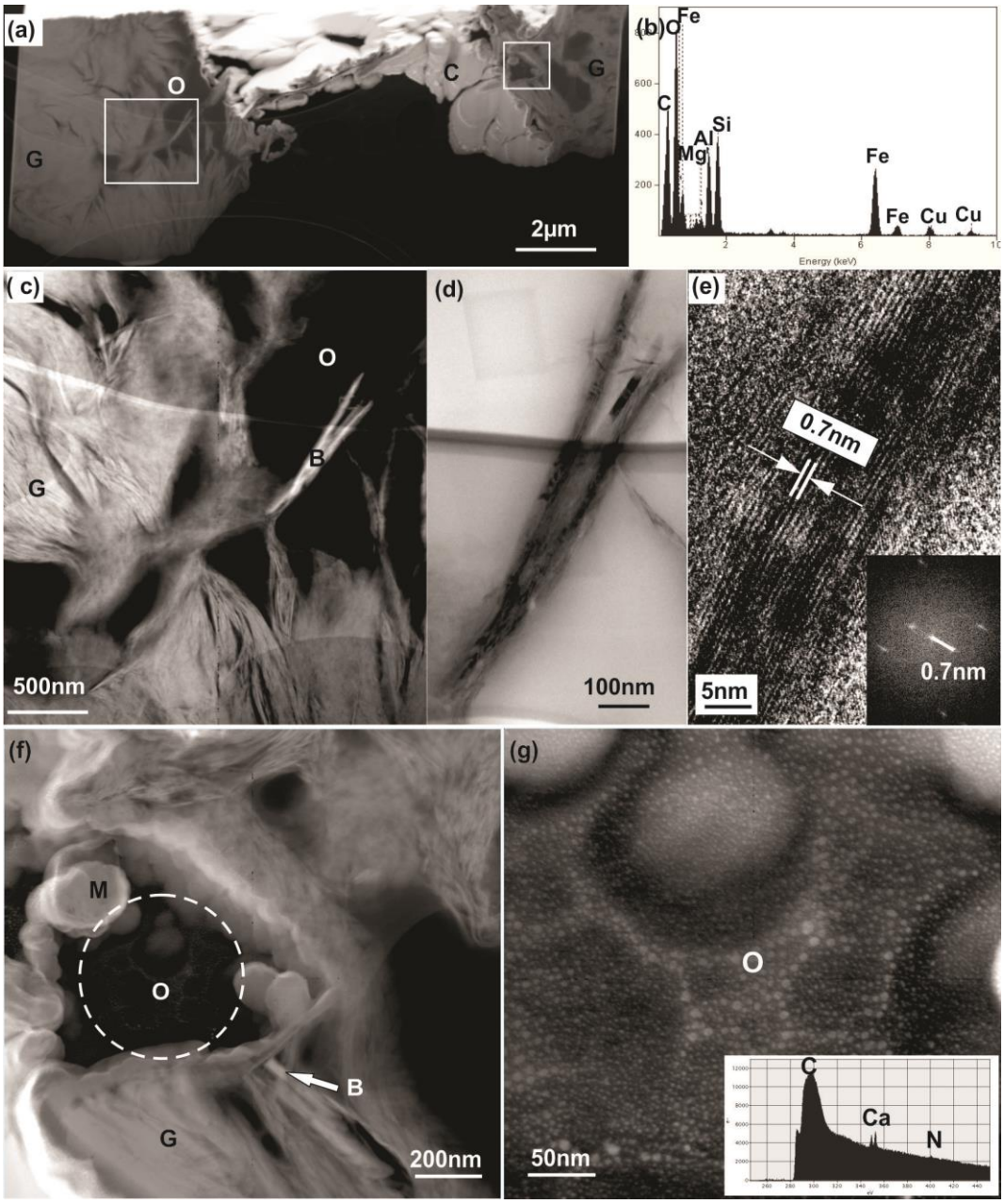

Figure 6. TEM investigations of berthierine type 1 and 4. Type 1 berthierine (6a-6e) coating glauconite grains in direct contact with residual oil. (a) High-magnification scanning transmission electron microscopy (STEM) image (high-angle annular dark-field [HAADF] mode) of a focused ion beam (FIB) foil. (b) EDS spectrum of berthierine in c.

(c) High resolution image of the left white rectangle in a. (d) Bright-field image of berthierine in c. (e) HRTEM micrograph of berthierine in d showing lattice fringes with 0.7 nm periodicity. The insert shows a SAED pattern with a pronounced 0.7nm periodicity. Type 3 berthierine (6e-6f) in transforming glauconite close to a mineralized oil water emulsion. (f) High resolution image of the right rectangle in a. Berthierine co-occurs with small Mn-oxide particles close to a mineralized oil-water emulsion (white dotted circle) in a glauconite pore. (g) High resolution image of the white circle in f shows small organic matter particles with carbon, calcium and nitrogen contents (illustrated in the inserted EELS spectrum). G: glauconite; B: berthierine; C: calcite; O: oil; M: Mn-Ti oxide. Well Siri-2, OWC.

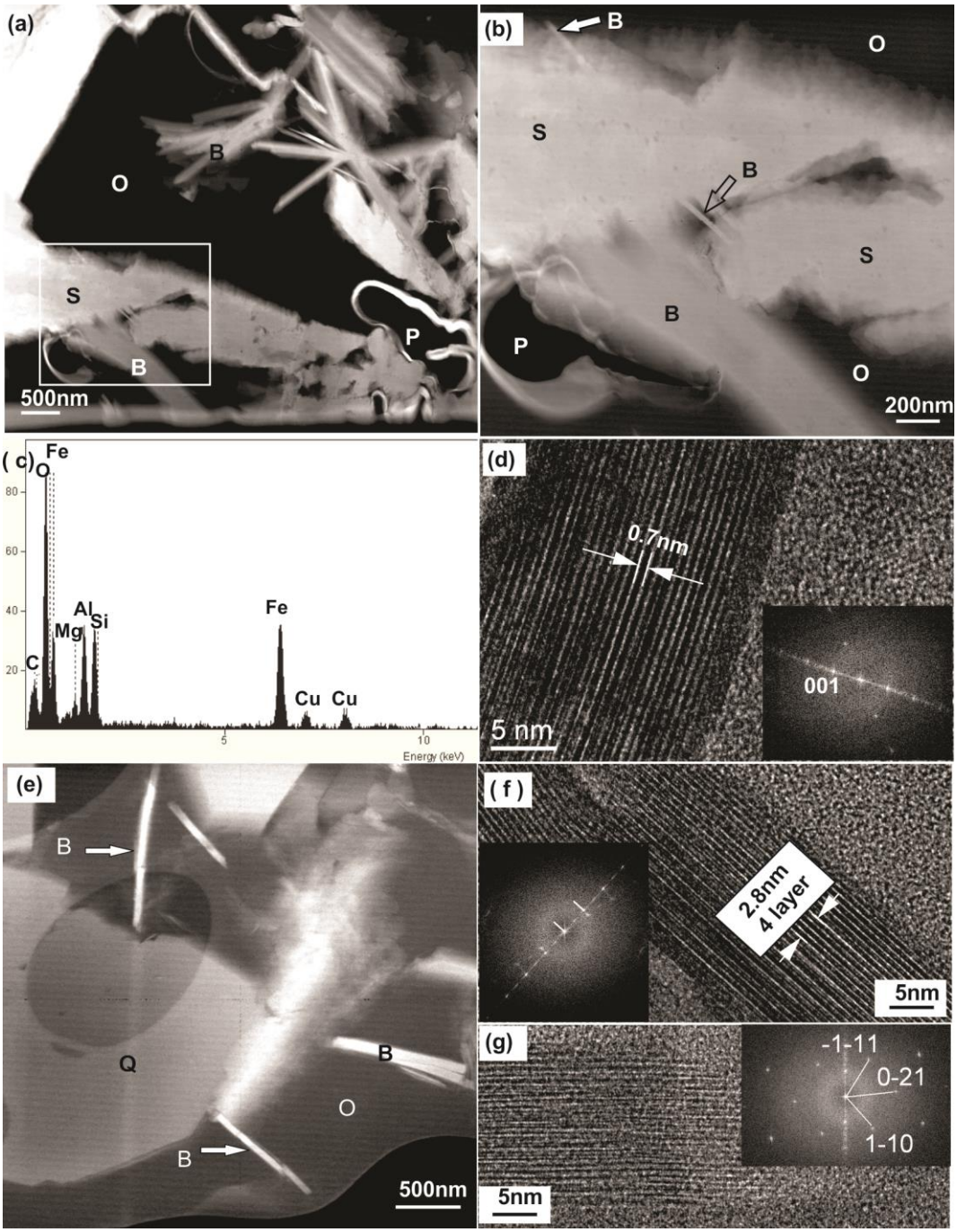

Figure 7. TEM investigations of berthierine type 5 (7a-7d) and type 2 (7e-7g). Type 5 berthierine (7a-7d) as blade-like particles in a siderite concretion. (a, b) High-magnification scanning transmission electron microscopy (STEM) images (high-angle annular dark-field [HAADF] mode) of a focused ion beam (FIB) foil extracted from the red rectangle in Figure 2b. (a) Growth of 1 µm large fibre-shaped berthierine in oil-filled pore. (b) High resolution image of the white rectangle area in a. Berthierine bridges siderite crystals. Additional berthierine (white arrow) is growing on a siderite

surface. (c) EDS analysis of the berthierine bridge marked by the black arrow in b. (d) HRTEM image of the berthierine bridge in b with the insert displaying its calculated diffraction pattern (fast Fourier Transform FFT) pattern of 0.7 nm periodicity. Type 2 berthierine (7e-7g) in open pore space filled by residual oil. (e) Several fibrous berthierine crystals in oil near an authigenic microquartz grain. (f) HRTEM micrograph of one fibrous berthierine crystal in e with well-defined 0.7 nm lattice fringes and SAED pattern of 0.7 nm periodicity (insert). (g) HRTEM image and SAED pattern (insert) of the upper left berthierine in e. S: siderite; B: berthierine; O: oil; P: pore; Q: microquartz. Figure 7a-7d: Well Siri-2, oil leg; Figure 7e-g: Well Siri-2, gas cap.

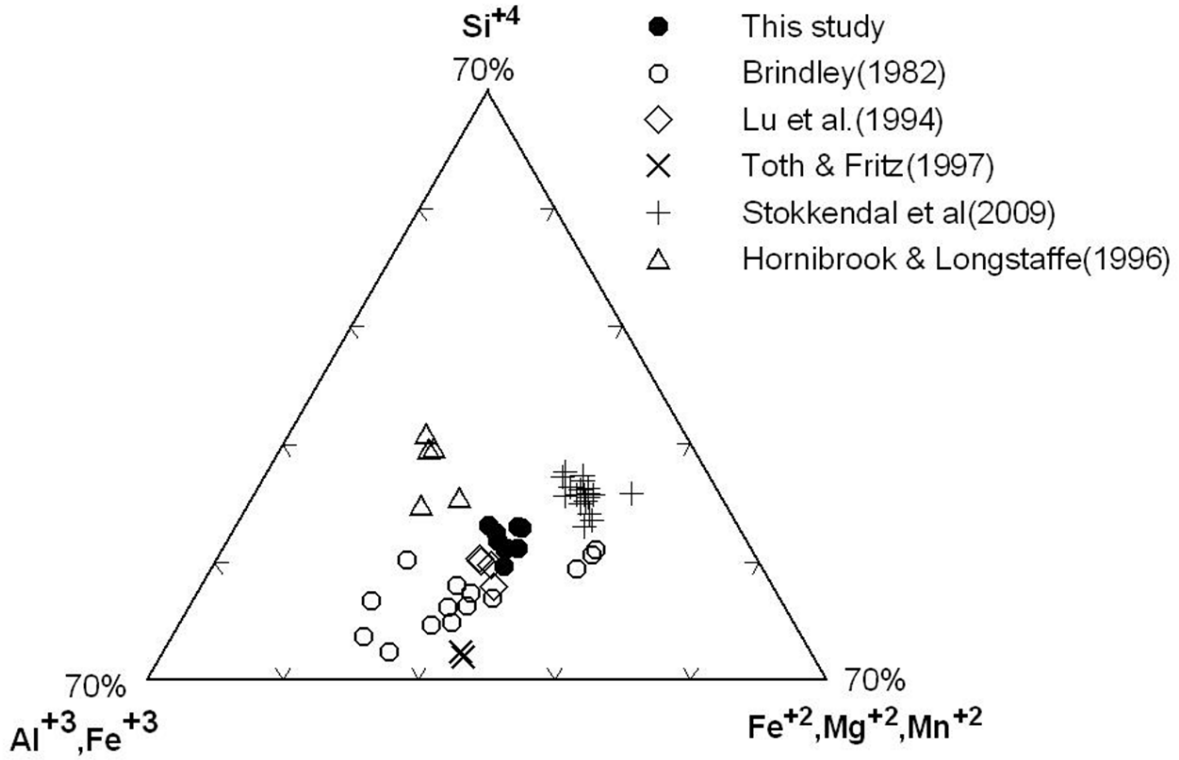

Figure 8. Measured cation composition of berthierine in a ternary plot in comparison with the results from other studies (Brindley, 1982; Hornibrook and Longstaffe, 1996; Lu et al., 1994; Stokkendal et al., 2009; Toth and Fritz, 1997).

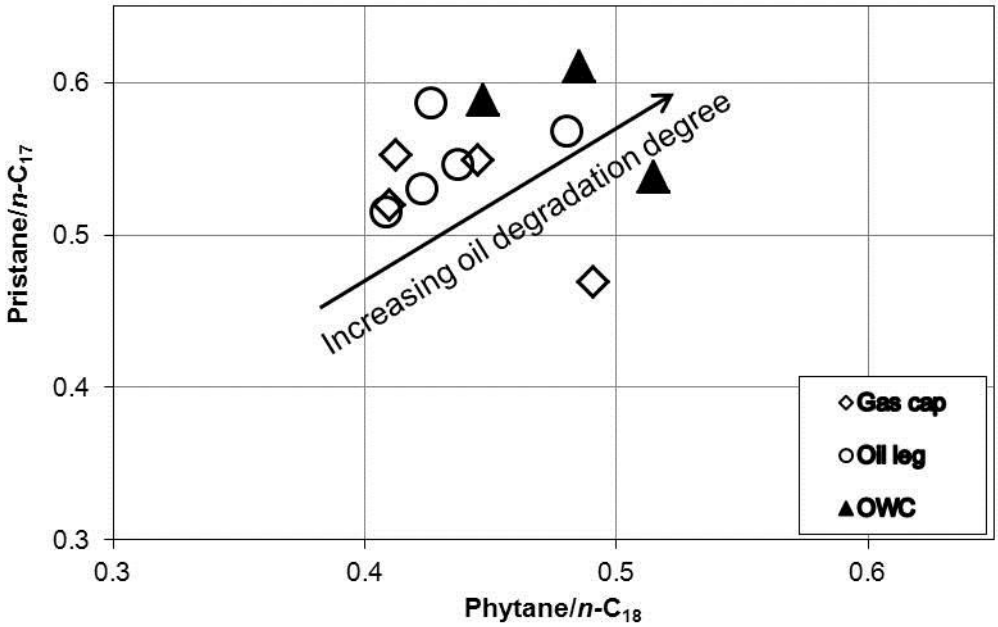

Figure 9. Plot of Pr/*n*-C17 versus Ph/*n*-C18 for 12 samples from the gas cap, the oil leg and OWC in well Siri-2.

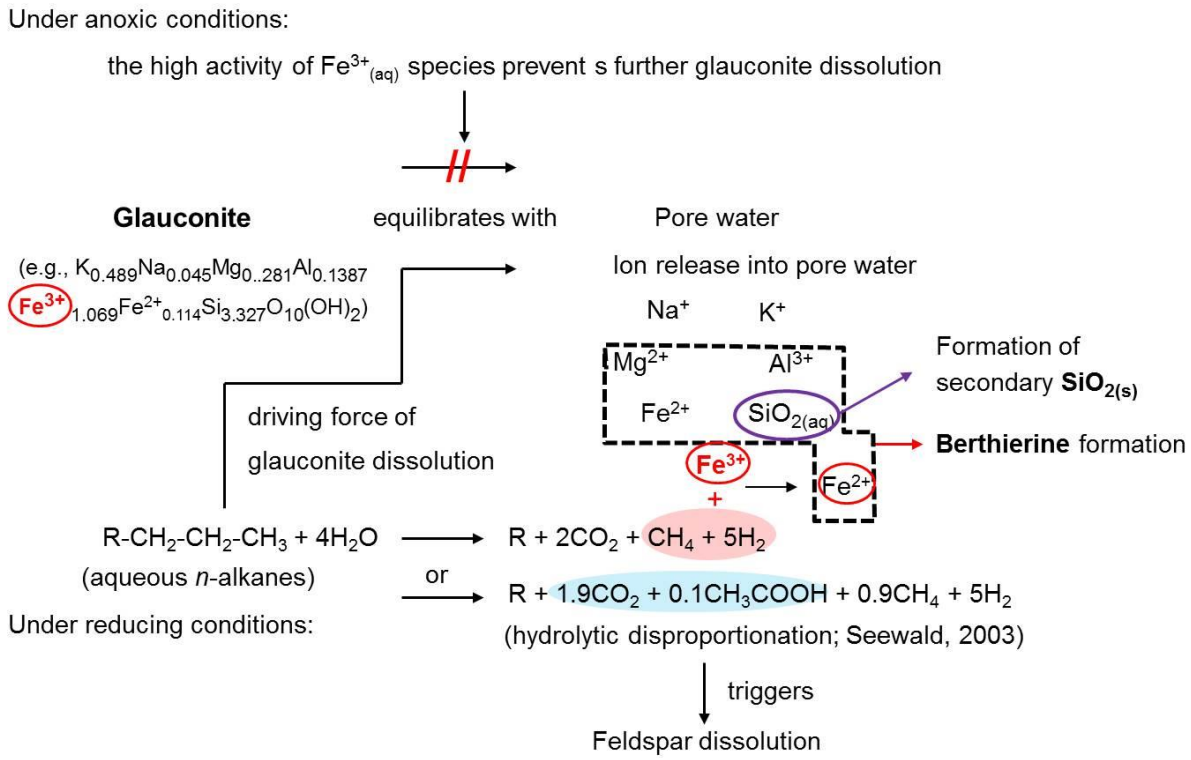

Figure 10. Conceptual model sketch as a result of observations showing berthierine formation and potential co-existing reactions in the Heimdal sandstone due to fluid-rock interactions trigged by oil degradation.